A new method for detecting aerosols: combining atmospheric detection LiDAR technology with intelligent driving technology

Hao Yang[1,2,3], Xiaomeng Zhu[1], Duoyang Qiu[1,2*], Xianyang Li[1], Zhiqiang Kuang[3],Zhiyuan Fang[5*], Yalin Hu[4,6]

[1]School of Advanced Manufacturing Engineering, Hefei University, Hefei 230601, China

[2]Anhui Provincial Engineering Technology Research Center of Intelligent Vehicle Control and Integrated Design Technology, Hefei University, Hefei 230601, China

[3]Hefei Innovation Institute, Hefei Institutes of Physical Science, Chinese Academy of Sciences, Hefei 230088, China

[4]University of Science and Technology of China, Hefei 230026, China

[5]School of Mechatronics and Energy Engineering, Ningbo Tech University, Ningbo 315100, China

[6]Anhui Institute of Optics and Fine Mechanics, Chinese Academy of Sciences, Hefei 230031, China

Corresponding author and email: Duoyang Qiu(qiudy@hfuu.edu.cn);

Zhiyuan Fang(fangzhy@mail.ustc.edu.cn)

Received: date; Accepted: date; Published: date

Abstract The existing aerosol mobile detection system has problems such as over-reliance on labor power and difficulty in conducting continuous operations in toxic and polluted environments. This paper presents a new method for detecting aerosols. The method combines atmospheric detection LiDAR technology and intelligent driving technology. Through modular design (including control module, aerosol detection module, environment sensing and positioning module, and wire control chassis module), an intelligent cruise detection system for aerosols was built. For path planning, Gaussian pseudo-spectrum method was used. The obstacle avoidance constraints and physical constraints during cruise detection movement was fully considered. Experiments were also conducted for three different application scenarios of continuous vertical detection, scanning detection and unmanned intelligent cruise detection. The experimental results show that the system can effectively and continuously acquire the vertical and spatial distribution of aerosol pollutants. It can achieve three-dimensional scanning and positioning tracking of atmospheric aerosols. It has the ability of unmanned cruise detection and real-time warning of regional pollution prevention and control. More detection experiments will be conducted in different environments in the future. We will continue to explore the application of this technology in intelligent cruise control, detection, and pollution prevention, providing new ideas for regional pollution monitoring.

Keywords: aerosol detection system; intelligent driving technology; LiDAR; regional pollution monitoring.

1. Introduction

Aerosols not only affect air quality (Monks et al., 2009), causing reduced visibility and leading to a

high incidence of traffic accidents(Gao et al., 2019), but also have an impact on climate(Kok et al., 2023). Some germs and viruses are spread by aerosols in the atmosphere; it has led to problems such as higher cancer rates and shorter life expectancy. This poses a serious threat to public health and daily life.(Oh et al., 2020; Pope Iii, 2002).

Among the current means of aerosols detection, LiDAR has ultra-high sensitivity, good temporal and spatial resolution, and the ability to capture targets in three dimensions(Eitel et al., 2016). It provides all-weather monitoring of clouds, aerosols, and atmospheric constituents(Cairo et al., 2024), making it widely used for atmospheric environment detection. According to different platforms, it is divided into Space-borne LiDAR, airborne LiDAR and ground-based LiDAR. Large scale and multi latitude atmospheric data can be obtained through space-borne LiDAR, which can provide data for areas that are difficult to observe on the ground.(Chen et al., 2023; Sun et al., 2024). Some scholars have used aerosol products from Space-borne LiDAR to study dust transport processes and surface characterization(Song et al., 2024; Yang et al., 2025). However, the construction costs and technical requirements of Space-borne LiDAR are high, and it is impossible to achieve continuous detection of a certain area. Airborne LiDAR is a LiDAR system mounted on aircraft or drones, capable of providing large-area coverage and highly mobile detection scanning. Some scholars employ airborne LiDAR to study the surface properties of desert aerosols, analyze marine aerosol concentration distributions, and the vertical distribution of urban pollution(Eckert et al., 2024; Li et al., 2022; Zhou et al., 2022), while others use it to measure the optical characteristics of particulate matter(Girdwood, 2023). However, the high cost and airspace limitations have hindered the continued use of airborne LiDAR. Ground-based LiDAR is widely used to detect aerosol pollution. It can achieve continuous fixed-point detection and effectively monitor the vertical airspace over a specific area(Yang et al., 2024). LiDAR fixed on a building for continuous fixed-point vertical detection(Kuang et al., 2023), it can capture of aerosol transport processes(Yang et al., 2021a). Zhang et al. used a ground-based lidar network to analyze a dust aerosol transport over northern China in 21 years(Zhang et al., 2024). LiDAR paired with a gimbal can carry out scanning detection. Horizontal scanning effectively captures contaminants within the detection distance. It enables pollutants to be effectively tracked and potential sources of contamination to be identified(Kuang et al., 2023). The cone scanning can detect the pollutants in the scanning area by stereoscopic scanning and provide strong data support(Xie et al., 2015). Vertical detection and scanning detection can only achieve fixed-point detection within a specific area, resulting in limited detection coverage. However, if ground-based LiDAR is mounted on a mobile platform, navigation detection can be achieved. It has the advantages of large detection range and long detection distance, and can perform large-scale mobile detection in urban areas.(Wang et al., 2024; Zhang et al., 2020). It is even possible to observe the optical characterization of pollutants in a geographic area on a continuously moving basis and to detect sources of pollution(Lv et al., 2017; Wang et al., 2009).

However, the need for uninterrupted cruise detection during regional pollution prevention and control actions, can lead to a significant loss of operator energy. This has resulted in a significant increase in labor costs for existing manned cruise detection systems. In addition, being in an environment with high concentrations of toxic pollutant emissions can cause irreversible damage to the bodies of researchers. In order to address the above issues, this paper presents a new method for detecting aerosols. The method combines atmospheric detection LiDAR technology and intelligent driving technology. The system can carry out unmanned cruise detection for long periods of time, providing a new way of thinking about regional pollutant monitoring. The second part introduces the system and research method. The third part analyzes the results of different experiments. The fourth part is summary and prospect.

2. Systems and research method

2.1 System Principles and Models

Intelligent cruise detection system for aerosols is shown in Fig. 1. The system comprises a control module, an aerosol detection module, an environment sensing and positioning module, and a wire control chassis module, and is integrated into a small electric unmanned vehicle. The control module is composed of industrial controller, computing platform, vehicle controller and gateway. The environment sensing and positioning module includes vehicle LiDAR, binocular camera, and an integrated navigation system (including GPS antenna and inertial navigation). The wire control chassis module consists of brake module, drive module and steering module.

The aerosol detection module and the unmanned vehicle system each have their own control units. As the "brain" of the whole system, the control module controls the operation of the whole system. The computing platform receives the localization data and environmental data detected by the environment awareness and localization module through the processing gateway. Based on this input, it’s dynamically computing the required gear ratio, velocity parameters, and braking force for the unmanned vehicle and transmits these values via the vehicle controller to the wire control chassis module. The wire control chassis module feeds back the state of the moving vehicle parameters (speed, acceleration, rotational speed and braking, etc.) to the computing platform. The environment sensing and positioning module communicates with the computing platform via the Internet, while the Drive-by-Wire Chassis Module communicates with it via the CAN bus. A Mie scattering LiDAR is selected for the aerosol detection module, mounted on the roof of the unmanned vehicle. The LiDAR system and the industrial controller form an integrated system. All modules within the LiDAR system communicate with the industrial controller via TCP/IP protocols over Ethernet/Wi-Fi networks. The inverter provides a stable 220V power supply to the LiDAR and computing platform. Fig.1b is the module distribution of the detection system. The relevant technical parameters of the system can be seen in Table1.

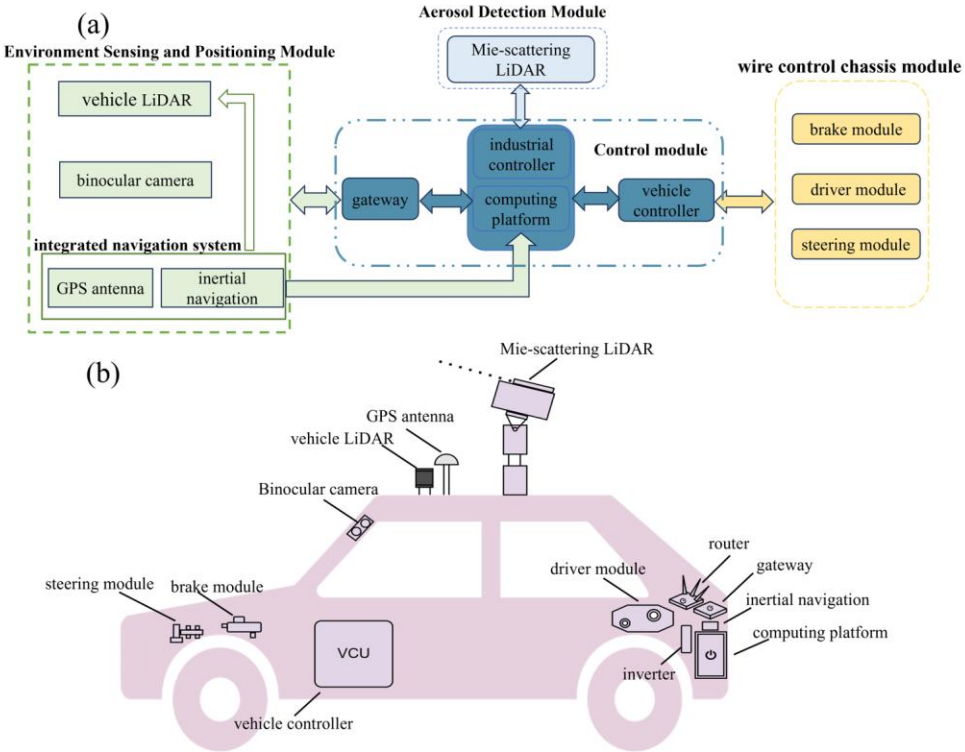

Fig. 1 Intelligent cruise detection system for aerosols: (a)The system schematic; (b) The module distribution of the detection system (this figure is an original creation by the authors).

Table 1 Relevant technical parameters of Intelligent cruise detection system for aerosols

	parameters	numerical value
Mie-scattering LiDAR Technical Parameters	laser wavelength	1064nm
	pulse energy	15μJ
	Pulse Repetition Frequency	10kHz
	Acquisition Channel	1800
	Distance resolution	7.5m
Unmanned Vehicle Technical Parameters	Wheelbases(L)	2.56m
	Vehicle front overhang(f)	0.902m
	Vehicle rear overhang(r)	0.883m
	body width(d)	1.765m

2.2 Aerosol detection methods

Mie-scattering LiDAR is commonly used to measure aerosols, which refers to laser radar systems engineered based on Mie scattering principles. It quantifies the optical properties of aerosol particles and clouds by receiving Mie-scattering echoes from these atmospheric constituents. **In reality, a Mie-scattering LiDAR receives the sum of Mie-scattering signals from aerosol particles and Rayleigh-scattering signals from air molecules. However, within the boundary layer, Mie-scattering is dominant, and Rayleigh-scattering can be neglected**(Megie, 1985)**.** The equation of LiDAR is (Yang et al., 2021b):

$$P(z)=\frac{C[\beta_m(z)+\beta_a(z)]\bullet e^{\{-2\int_0^z[\alpha_m(z')+\alpha_a(z')]dz'\}}}{z^2} \tag{1}$$

In the formula (1), *P(z)* is the received echo signal of height z, C is the LiDAR constant. βm and βa are the backscattering coefficients of atmospheric molecules and aerosols respectively. α_m and α_a are the extinction coefficients of atmospheric molecules and aerosol molecules, respectively. z is the height of aerosol LiDAR detection.

In order to make the detection results more accurate, the Range-corrected signal is usually used:

$$X(z)=P(z)\bullet z^2 \tag{2}$$

2.3 Kinematic Model of Unmanned Vehicle and Obstacle Avoidance Constraints

Considering experimental safety, the speed is maintained at a low level, all wheels are in a rolling state, and the influence of lateral force is ignored; vehicle dynamics are ignored, so only the vehicle kinematic model is considered.

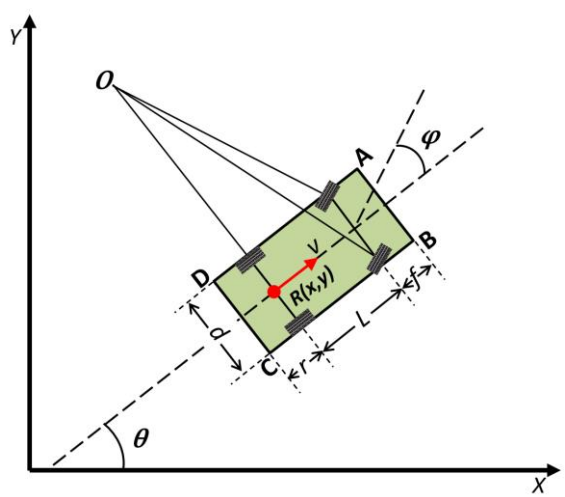

Fig. 2 The kinematic model of the vehicle.

In Fig. 2. L, f, r and d are the wheelbase, front overhang, rear overhang and width of the vehicle respectively; point R(*x, y*) is the center of the rear axle of the vehicle; *v* is the velocity of point R along the longitudinal axis of the vehicle; O is the instantaneous steering center of the vehicle; φ is the

equivalent swing angle of the front wheel; θ is the heading angle of the vehicle; A, B, C and D are the four contour vertices of the vehicle body respectively.

During the vehicle movement process, the state variables of point R(x, y) in the ground coordinate system include: lateral displacement x, longitudinal displacement y, velocity of the rear axle center point v, vehicle acceleration a, vehicle heading angle θ, and equivalent swing angle of the front wheel φ; The control variables include the vehicle acceleration rate j and the angular velocity of the front wheel's equivalent swing angle ω. Thus, the kinematic differential equations of the vehicle can be obtained as follows:

$$\frac{d}{dt}\begin{bmatrix} x(t) \\ y(t) \\ v(t) \\ a(t) \\ \theta(t) \\ \varphi(t) \end{bmatrix} = \begin{bmatrix} v(t)\bullet\cos\theta(t) \\ v(t)\bullet\sin\theta(t) \\ a(t) \\ j(t) \\ v(t)\bullet\tan\varphi(t)/L \\ \omega(t) \end{bmatrix}, t \in [t_0, t_f] \tag{3}$$

In the formula (3): t_0 and t_f are the initial and termination moments respectively of the unmanned vehicle respectively.

Unmanned vehicles need to satisfy their own physical and mechanical constraints while traveling. This is translated into inequality constraints on some of the state and control variables as follows:

$$\begin{cases} |v(\mathrm{t})| \le v_{\max} \\ |\mathrm{a(t)}| \le \mathrm{a}_{\max} \\ |\mathrm{j(t)}| \le \mathrm{j}_{\max} \quad , t \in [t_0, t_f] \\ |\varphi(t)| \le \varphi_{\max} \\ |\omega(t)| \le \omega_{\max} \end{cases} \tag{4}$$

In Formula (4), v_{max} is the maximum permissible speed during driving, a_{max} is the maximum acceleration allowed during driving, j_{max} is the maximum rate of change of acceleration allowed during driving, φ_{max} is the maximum allowable front wheel equivalent swing angle, ω_{max} is the maximum allowable front wheel swing angle angular velocity.

Vehicle collision avoidance constraints are important when solving trajectory planning problems. The actual top-view projection shape of the vehicle is close to a rectangle. Here the vehicle contour is depicted with an enlarged rectangle. d_{safe} is the safety threshold to ensure that the vehicle is collision free.

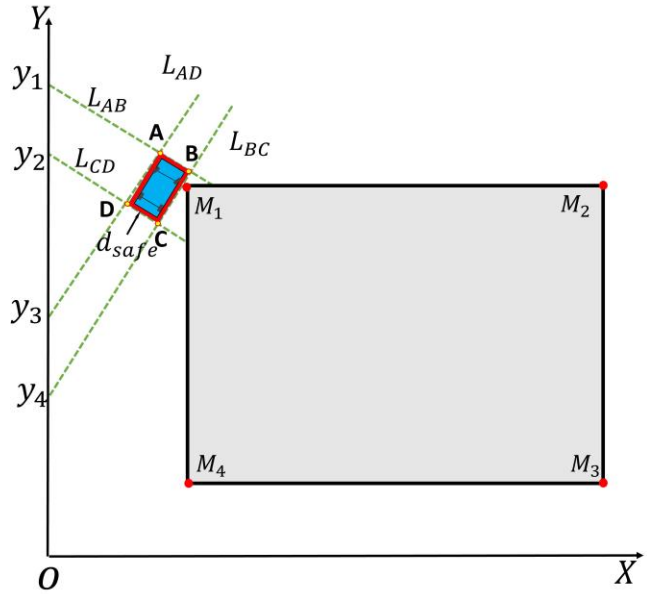

Fig. 3 Schematic diagram of obstacle avoidance constraints.

As shown in Fig. 3. The red area around the vehicle is the safety threshold to ensure a collision-free vehicle. If the vehicle does not collide with point *M* while traveling, the point *M* coordinates are always outside the rectangular *ABCD* region. Remember that the four sides of the rectangle are the lines L_{AB}, L_{BC}, L_{CD}, and L_{AD}, and their linear equations are as follows:

$$\begin{cases} L_{AB} = k_1 \bullet x + y_1 \\ L_{CD} = k_1 \bullet x + y_2 \\ L_{AD} = k_2 \bullet x + y_3 \\ L_{BC} = k_2 \bullet x + y_4 \end{cases} \tag{5}$$

k_1 is the slope of the lines L_{AB}, and L_{CD}, k_2 is the slope of the lines L_{AD}, and L_{BC}. If the line L_{AB} is parallel or perpendicular to the X-axis so that the point *M* is outside the rectangle *ABCD*, then the coordinates of the point *M* must satisfy the following conditions:

$$\begin{cases} M_{ix} < D_x(t) \text{or } M_{ix} > A_x(t) \text{or } M_{iy} < C_y(t) \text{or } M_{iy} > A_y(t), \theta = 0^\circ \\ M_{ix} < D_x(t) \text{or } M_{ix} > C_x(t) \text{or } M_{iy} < D_y(t) \text{or } M_{iy} > A_y(t), \theta = 90^\circ \\ M_{ix} < A_x(t) \text{or } M_{ix} > D_x(t) \text{or } M_{iy} < D_y(t) \text{or } M_{iy} > C_y(t), \theta = 180^\circ \\ M_{ix} < D_x(t) \text{or } M_{ix} > C_x(t) \text{or } M_{iy} < A_y(t) \text{or } M_{iy} > D_y(t), \theta = 270^\circ \end{cases} \tag{6}$$

In the formula (6), (i = 1, 2, 3, 4 represent the four vertices of the rectangle). For a line L_{AB} that is neither parallel nor perpendicular to the X-axis, if point *M* lies outside the quadrilateral *ABCD*, the following conditions must hold:

$$\begin{cases} (M_{iy} - k_1 \bullet M_{ix}) < y_2 \text{ or } (M_{iy} - k_1 \bullet M_{ix}) > y_1 \\ (M_{iy} - k_2 \bullet M_{ix}) < y_4 \text{ or } (M_{iy} - k_2 \bullet M_{ix}) > y_3 \end{cases} \tag{7}$$

2.4 Unmanned Mobile Detection Path Planning Algorithm

In this paper, the segmented Gaussian pseudo-spectral method was used, which has the advantages of faster convergence and high success rate of solution. Gaussian pseudo-spectral method is a direct method for solving nonlinear optimal control problems. The method constructs Lagrange interpolation polynomials to approximate the state and control variables after discretizing the continuous optimization problem at the Legendre-Gauss (LG) collocation point. And replace the differential equation constraints with algebraic constraints, thus transforming the optimal control problem into a Nonlinear Programming (NLP) problem to be solved. Qiu et al. proposed a hierarchical trajectory planning and tracking control algorithm for unmanned vehicles combining Model Predictive Control (MPC) and Gaussian Pseudo-spectral Method (GPM). (Qiu et al., 2021).

An optimal control problem typically comprises: the system dynamics differential equations, physical constraints, obstacle avoidance constraints, boundary constraints, and a performance index function. The optimal control parameters are obtained by minimizing the performance index function while satisfying all constraints. **The Bolza problem in nonlinear optimization is one of the main problems in classical calculus of variations that deals with the conditions for extreme points under certain constraints(Wang et al., 2021). This problem has a special feature of the mixed nature of the functional represented as the sum of an integral functional and a function on the boundary. It not only emphasizes the system state at the terminal moment, but also stresses the requirements for the control system process.** Without loss of generality, the Bolza problem for nonlinear optimal control can be described as:

$$\min \psi = \phi(\xi(t_0), t_0, \xi(t_f), t_f) + \int_{t_0}^{t_f} g(\xi(t), \mu(t), t)dt \tag{8}$$

In the formula (8): $\xi(t)$ and $\mu(t)$ are the state and control variables of the system, respectively. The state variables $\xi(t)$ encompass the vehicle's longitudinal displacement x, lateral displacement y, velocity v, acceleration a, heading angle θ, and wheel steering angle φ. The control variables include the wheel angular velocity ω and jerk. $\xi(t) \in R^n$ and $\mu(t) \in R^m$ satisfy.

$$s.t. \begin{cases} \dot{\xi}(t) = f(\xi(t), \mu(t), t) \\ M(\xi(t), \mu(t), t) \le 0 \qquad t \in [t_0, t_f] \\ N(\xi(t_0), t_0, \xi(t_f), t_f) = 0 \end{cases} \tag{9}$$

In the formula (9): The first behavior describes the differential equation of state of the system. The second behavior is an inequality constraint on the system variables during the solution of the objective function. The third behavior is an equational constraint on the system variables during the solution of the objective function. Given environmental perception data, the objective function of the optimal control problem is formulated to minimize task completion time for autonomous driving.

Based on the above context, the nonlinear optimal control problem for vehicle trajectory planning can be described as follows: the objective is to minimize t_f, that is min t_f. Meanwhile, within the time interval t $\in[t_0, t_f]$, the vehicle system must satisfy the state differential equations, physical system constraints, obstacle avoidance constraints, and boundary condition constraints.

The following is the solution for vehicle trajectory based on the Gauss Pseudospectral Method (GPM).

(1) time-domain transformations: The initial-final time domain t$\in[t_0,t_f]$ is partitioned into U subintervals. In the GPM algorithm, the intervals of time-variable discrete points are $\tau \in [-1,1]$, so the subinterval moments need to be transformed in the time domain. For any arbitrary time instant t$\in$[tv-1, tv] within the v-th subinterval, conversion by expression to $\tau \in [-1,1]$.

$$\tau = \frac{2 \bullet t - (t_{\text{v-1}} + t_v)}{t_v - t_{\text{v-1}}} \tag{10}$$

After time-domain transformation, the optimal control problem within subinterval x can be formally stated as follows:

$$\min \psi^{(v)} = \phi^{(v)}(\xi^{(v)}(\tau_0), t_{v-1}, \xi^{(v)}(\tau_f), t_v) + \frac{t_v - t_{\text{v-1}}}{2} \int_{\tau_0}^{\tau_f} \text{g}(\xi^v(\tau), \mu^{(v)}(\tau), \tau : t_{\text{v-1}}, t_v) d\tau \tag{11}$$

$$s.t. \begin{cases} \dot{\xi}^{(v)}(\tau) = \dfrac{t_v - t_{v-1}}{2} f(\xi^{(v)}(\tau), \mu^{(v)}(\tau), \tau : t_{v-1}, t_v) \\ M(\xi^v(\xi), \mu^{(v)}(\tau), \tau : t_{v-1}, t_v) \le 0 \qquad\qquad \tau \in [-1,1] \\ N(\xi^{(v)}(\tau_0), \tau_0, \xi^{(v)}(\tau_f), \tau_f) = 0 \end{cases} \tag{12}$$

In the formula (12), $\xi^{(v)}(\tau)$ and $\mu^{(v)}(\tau)$ represent the state variable and control variable, respectively, after time-domain transformation at time t in the v-th subinterval $[t_{v-1}, t_v]$.

(2) variable discretization: Discretize the state and control variables at Legendre-Gauss (LG) collocation points and construct Lagrange polynomial approximations to represent the states ξ and controls μ during the maneuvering process. Legendre polynomials of order N on the interval $[\tau_0, \tau_f]$ are:

$$P_N(\tau) = \frac{1}{2^N \bullet N!} \times \frac{d^N}{d\tau^N} \bullet [(\tau^2 - 1)^N] \tag{13}$$

With the zeros $(\tau_1, \tau_2, \tau_3, \ldots, \tau_N)$ and the initial point τ_0 forming the constellation of N+1 collocation points, the state and control variables at each collocation point are defined as:

$$\begin{cases} \xi(\tau_0), \xi(\tau_1), \ldots, \xi(\tau_N) \\ \mu(\tau_0), \mu(\tau_1), \ldots, \mu(\tau_N) \end{cases} \tag{14}$$

At $N+1$ collocation points, construct a Lagrange interpolating polynomial using the following basis functions.

$$\begin{cases} L_i(\tau) = \prod_{j=0, j\neq i}^{N} \frac{\tau - \tau_j}{\tau_i - \tau_j} \\ \tilde{L}_i(\tau) = \prod_{j=0, j\neq i}^{N} \frac{\tau - \tau_j}{\tau_i - \tau_j} \end{cases} \tag{15}$$

The approximate polynomials for the state variables, control variables, are expressed as follows:

$$\begin{cases} \xi^{(v)}(\tau) \approx \sum_{i=0}^{N} L_i^{(\mu)}(\tau) \bullet \varsigma^{(v)}(\tau_i) \\ \mu^{(v)}(\tau) \approx \sum_{i=0}^{N} \tilde{L}_i^{(\mu)}(\tau) \bullet U^{(v)}(\tau_i) \end{cases} \tag{16}$$

By differentiating the aforementioned expression, the derivative of the state variable can be approximated using the derivative of the interpolation polynomial. For example, the derivative of the state variable at a time point can be expressed as:

$$\dot{\xi}^{(u)}(\tau_k) \approx \sum_{i=0}^{N} L_i^{(u)}(\tau_k) \bullet \varsigma^{(v)}(\tau_i) \tag{17}$$

Transformation of kinematic differential equation constraints into algebraic equality constraints:

$$\dot{\xi}^{(u)}(\tau_k) - \frac{t_v - t_{v-1}}{2} f(\varsigma(\tau_k), U(\tau_K), \tau_K) = 0 \tag{18}$$

(3) Under discretization, the equality and inequality constraints for system variables are formulated respectively as:

$$\begin{cases} M(\varsigma^{(v)}(\tau_k), U^{(v)}(\tau_k), \tau_k : t_{v-1}, t_v) \leq 0 \\ N(\varsigma^{(v)}(\tau_0), \tau_0, \varsigma^{(v)}(\tau_f), \tau_f) = 0 \end{cases} \tag{19}$$

Through the discretization, the optimal control problem of vehicle trajectory planning can be transformed into a nonlinear programming problem. Performance metrics can be obtained for discrete conditions:

$$\min \psi^{(v)} = \phi^{(v)}(\xi^{(v)}(\tau_0), t_{v-1}, \xi^{(v)}(\tau_f), t_v) + \frac{t_v - t_{v-1}}{2} \sum_{k=0}^{N} \rho_k \bullet g(\varsigma(\tau_k), U(\tau_k), \tau_k) \tag{20}$$

In summary, through discretization at the collocation points, the Bolza optimal control problem is transformed into a standard nonlinear programming (NLP) problem. This establishes the foundation for subsequent approximate solving of optimal control problems.

3 Experimental results and analysis

3.1 Vertical Detection

We carried out an outdoor fixed point continuous detection on February 24, 2025. Fig. 4a shows the Range-corrected signal data of that day. The Range-corrected signal can indicate the change in aerosol pollutant concentration on the same day. In Fig.4a, the temporal evolution of the vertical distribution of the near-surface aerosol layer is illustrated. The height of the aerosol layer was maintained at about 1.5 km for a long period of time. The aerosol concentration is relatively high below 1 km, the pollution concentration value decreases with the change of time from about 1 W·km² to 0.2 W·km²~0.3 W·km². Clouds were also detected at 2km to 2.5km.

Many previous studies have correlated multi-source data with LiDAR data to investigate variations in aerosol concentration(Tu et al., 2022; Xiao et al., 2023). In order to verify the accuracy of the system's detection, we also selected the hourly particulate matter concentration observed at the ground station in Hefei City on February 24th. Fig. 4b shows the variation curve of particulate matter concentration on the 24th (daily average concentration thresholds of 150μg/m^3 and 75μg/m^3 for PM_{10} and $PM_{2.5}$, respectively). When the $PM_{2.5}/PM_{10}$ ratio is below 0.5, it means large particle pollutants account for the main part of the air. When the ratio is 0.5 or above, it indicates that air pollution is dominated by fine particle pollutants.$PM_{2.5}$ and PM_{10} concentrations were higher than 100μg/m^3 from 0:00 to 5:00. $PM_{2.5}/PM_{10}$ values were around 0.8, indicating that the pollution in this phase is local fine particulate matter. Then, the three curves dropped rapidly reaching a minimum at 10:00(56μg/m^3 for PM_{10};23μg/m^3 for $PM_{2.5}$ and 0.41 for $PM_{2.5}/PM_{10}$). At 16:00, the subsequent concentrations all rebounded, and the $PM_{2.5}/PM_{10}$ value stabilized between 0.5 and 0.6. The changes in particulate matter concentration data are consistent with the results of LiDAR detections. By retrieving the MERRA-2 reanalysis data (Fig. 5), it can be seen that Hefei experienced an aerosol pollution process from the 22nd to the 24th (UTC time). Through vertical detections and comparative analysis, we can obtain a more refined vertical distribution of aerosols from the LiDAR results.

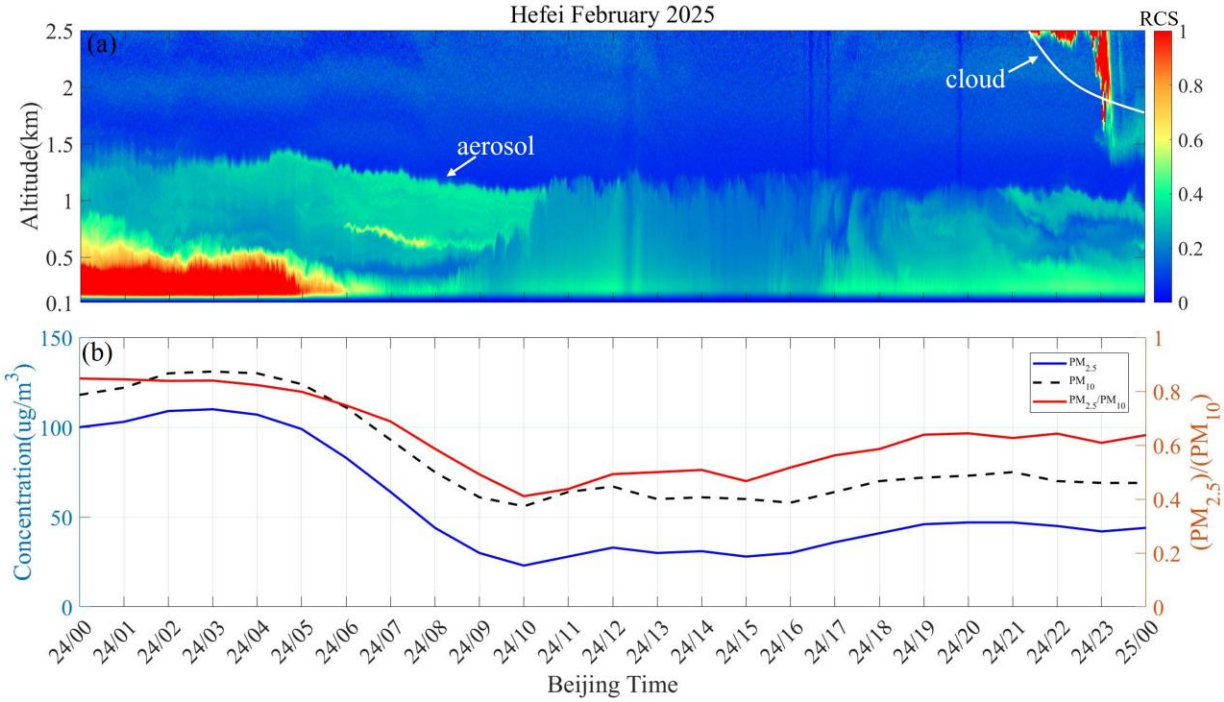

Fig. 4 Temporal variations in pollutant on 24 February: (a) The Range-corrected signal (W·km²) from Mie-scattering LiDAR;(b) The concentration of particulate matter at the ground station (the blue line indicates $PM_{2.5}$, the black line segment indicates PM_{10}, and the red line indicates $PM_{2.5}/PM_{10}$).

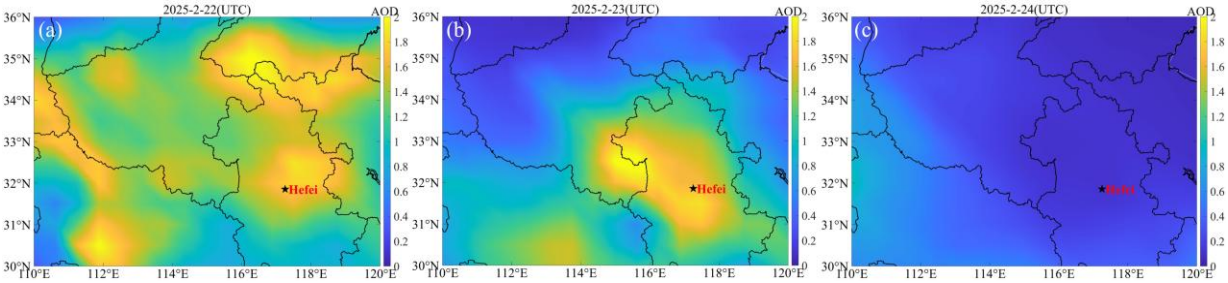

Fig. 5 MERRA-2 Aerosol Optical Depth Analysis: (a) The results of February 22, 2025; (b) The results of February 23, 2025; and (c) The results of February 24, 2025.

3.2 Cone-Scanning Detection

We conducted cone-scanning detection experiments on February 28, March 5, and March 6, 2025, respectively. The 0° direction is due west and the pitch angle is 75°, and the Range-corrected data were optioned for a range of 2.5 km. Fig. 6. shows the Range-corrected signal of cloudy days (February 28), polluted days (March 5) and clean days (March 6). From the Fig. 6 We can see the presence of clouds at 1.7km to the southeast (180°~240°) on the 28th, and the presence of aerosol air masses at about 0.67km at the point with a small concentration. Thin clouds were distributed near the ground (around 0.85km) on the 5th. Compared with the other two days, the aerosol air mass at the location on the 5th was widely

distribute. The system can achieve three-dimensional scanning and positioning tracking of atmospheric aerosols.

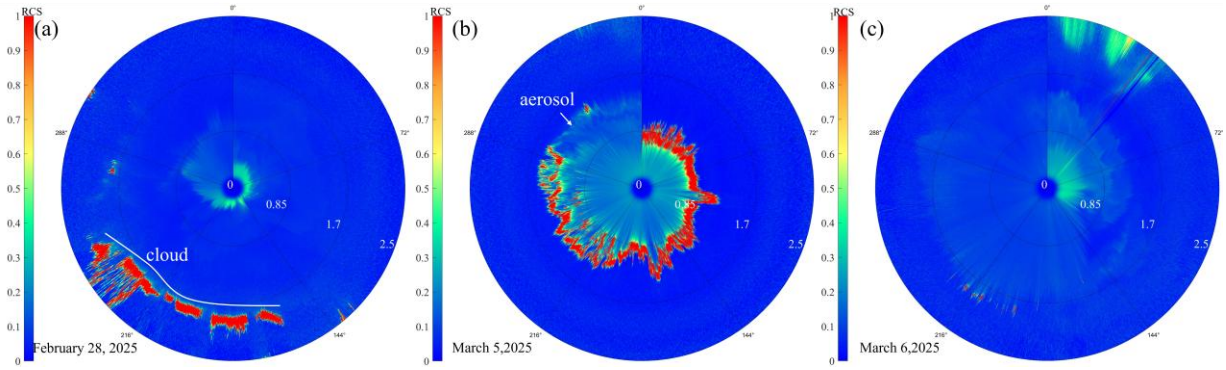

Fig. 6 Range-corrected signal(W·km²) from cone-scanning detection:(a) The results of February 28, 2025; (b) The results of March 5, 2025; and (c) The results of March 6, 2025.

3.3 Unmanned Intelligent Cruise Detection

We did an unmanned intelligent cruise detection experiment on February 26th. The location of the experiment was chosen near a laboratory building within the school. See Table 1 for unmanned vehicle parameters. The physical constraints are shown in Table 2. Fig. 7 shows the validation and simulation analysis of the trajectory planning algorithm based on the Gaussian pseudo-spectral method. Through simulation and emulation, we can achieve obstacle avoidance during the cruising detection process, and ensure safe and normal cruising according to the planned path.

Before the experiment, enter the Mie-scattering LiDAR system to configure the relevant detection parameters. This is followed by turning on the wire control chassis module of the unmanned vehicle and the modules related to the environment sensing and positioning module. Finally, the planned path is selected and the vehicle switches to autopilot.

Fig. 8 shows a plot of the Range-corrected signal from one unmanned cruise detection. On the day of the experiment, the air status index (AQI) of Hefei was 115, $PM_{2.5}$ was 80μg/m^3, and PM_{10} was 100μg/m^3(Data from China Environmental Monitoring Station;**http://106.37.208.233:20035**). It can be seen from Fig. 8a that the aerosol layer was about 0~0.3km. Pollution concentrations gradually decreased with time from 0.8 W·km² to about 0.2 W·km². The height of the aerosol layer rose to about 0.5 km in the later stages of the experiment. The results show that the system has the ability of unmanned cruise detection and real-time warning of regional pollution prevention and control.

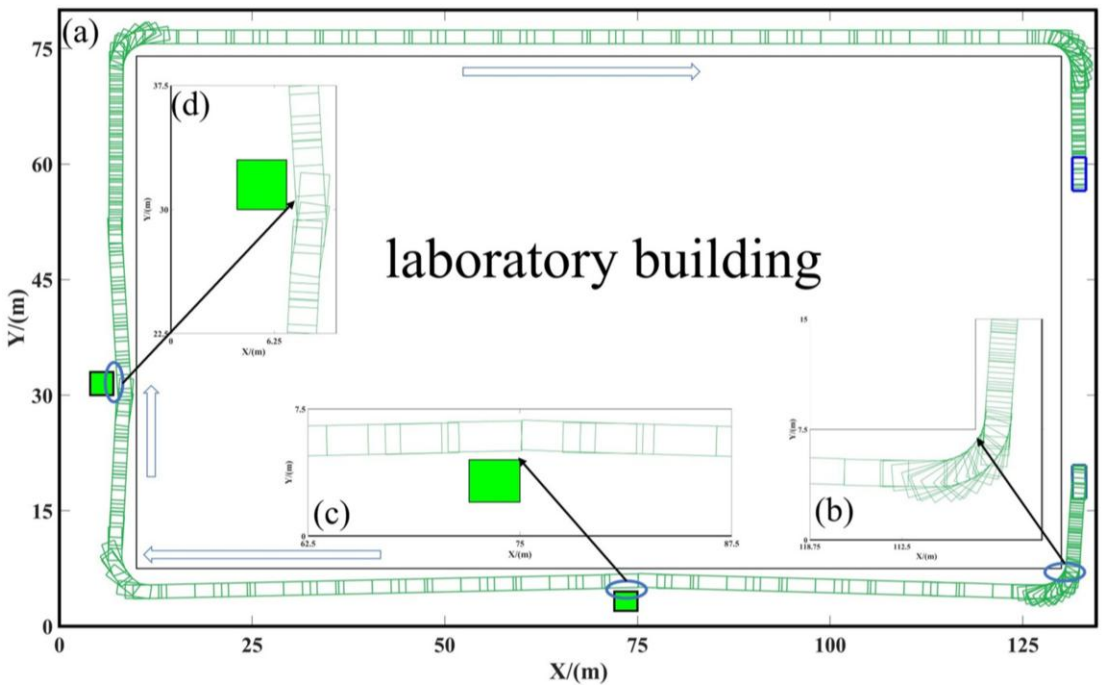

Fig. 7 Simulation of Cruise Detection Path Planning:(a) Navigation mobile route map; (b), (c) and (d) The simulation of obstacle avoidance for cornering, obstacle 1 and obstacle 2, respectively.

Table 2 Physical constraints for unmanned vehicles

Physical Constraints for Unmanned Vehicles					
parameters	v_{max}	a_{max}	j_{max}	φ_{max}	ω_{max}
numerical value	1.0m/s	0.1m/s^2	0.5m/s^3	0.56rad	0.56rad/s

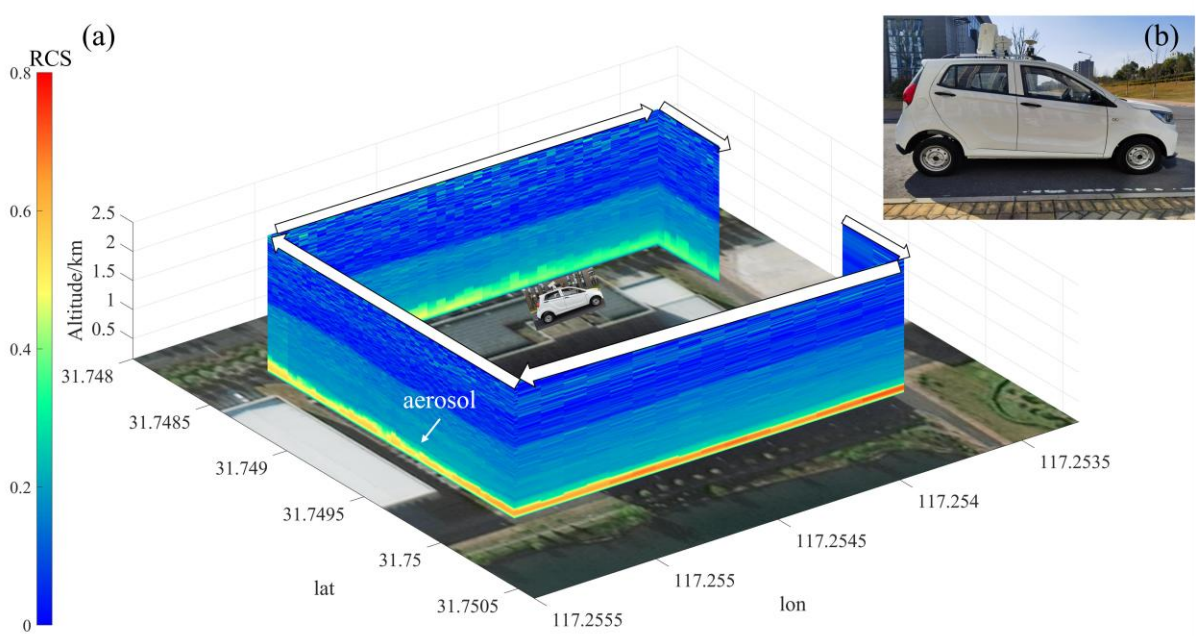

Fig. 8 Range-corrected signal (W·km²) superimposed on the map:(a) A map of Range-corrected signal for unmanned move detection (arrows are in the direction of vehicle travel); (b) An unmanned vehicle undergoing an unmanned walking experiment. (The map is a simple block map, ©2025Baidu-GS (2023)3206.)

4 Conclusions and outlook

We propose a new approach to aerosol detection that combines atmospheric detection LiDAR technology and smart driving technology. The intelligent cruise detection system for aerosols was built through a modularized design. The system includes: a control module, an aerosol detection module, an environment sensing and positioning module, and a wire control chassis module. Firstly, continuous vertical detection experiments show that the system can continuously observe the vertical distribution of aerosols for a long time (24 hours). And it can provide the fine structure of clouds and aerosols from 0-2.5km. Through analysis, the variation of aerosol pollution in the detection area can be obtained. In addition, through scanning detection, the system has long-term 0-360° scanning detection capability. The system is capable of effective detection of different weather conditions (clean, polluted and cloudy days). Finally, an unmanned intelligent cruise detection experiment is conducted. The results of the experiment showed that the aerosol height increased from 0.3km to 0.5km on the day of the experiment and the pollution concentration gradually decreased from 0.8 W·km² to about 0.2 W·km². It shows that the system is capable of stable unmanned cruise detection and has ability to monitor the concentration and spatial distribution of pollutants. Experimentally demonstrated in three different ways: the system can obtain the vertical and spatial distribute on of aerosol pollutants effectively and continuously; it can achieve three-dimensional scanning and positioning tracking of atmospheric aerosols; it has the capability of unmanned cruise detection and real-time warning of regional pollution prevention and control.

Our team realized multi-sensor fusion. The safety and effectiveness of this method are verified by the experiments of three application scenarios in the park. In the future, we will expand the scope of the detection area and conduct different detection experiments for different pollution scenarios. Intelligent cruise detection for complex scenes will also be further optimized in our subsequent long-term experiments. We will continue to explore the application of relevant technologies in intelligent cruise, detection and pollution prevention, and provide new ideas for regional pollution monitoring.

Declaration of Competing Interest

The authors declare no conflict of interest.

Data availability

The LiDAR data presented in this study are available from the corresponding author upon request(yh9599@mail.ustc.edu.cn). Particulate matter concentration data from China Environmental Monitoring Station for providing the particulate matter data(**http://106.37.208.233:20035**). MERRA-2 provides Aerosol Optical Depth Analysis data(**https://gmao.gsfc.nasa.gov/reanalysis/MERRA-2/**).

Financial support

This work is jointly funded by the National Science Foundation of China (Grant No. 42405069), the University Natural Sciences Research Project of Anhui Province (Grant No. 2023AH052201 and 2023AH052184), the 2023Talent Research Fund Project of Hefei University (No.23RC01), and the Technical Development Project of Hefei University (No.902/22050124128, No.902/22050124148, No.902/22050124149, and No.902/22050124250).

Author Contributions

Supervision, HY; designed the study, XMZ; Methodology, XMZ; Software, HY and ZQK, DYQ, ZYF; XMZ and XYL; Writing–original draft, XMZ; Writing–review & editing, YLH, ZYF, XMZ, XYL, DY Q and HY.

Reference

Monks P S, Granier C, Fuzzi S, et al. Atmospheric composition change–global and regional air quality. Atmospheric environment.,43, 5268–5350. https://doi.org/10.1016/j.atmosenv.2009.08.021., **2009**.

Gao, K.; Tu, H.; Shi, H. Stage-Specific Impacts of Hazy Weather on Car Following. Proceedings of the Institution of Civil Engineers – Transport., 172 (6), 347–359. https://doi.org/10.1680/jtran.16.00182., **2019**.

Kok J F, Storelvmo T, Karydis V A, et al. Mineral dust aerosol impacts on global climate and climate change[J]. Nature Reviews Earth & Environment, 4(2): 71-86., **2023**.

Oh H, Ma Y, Kim J. Human Inhalation Exposure to Aerosol and Health Effect: Aerosol Monitoring and Modelling Regional Deposited Doses[J]. International Journal of Environmental Research and Public Health, 17(6)., **2020**.

III P A C, Burnett T R, Thun J M, et al. Lung Cancer, Cardiopulmonary Mortality, and Long-Term Exposure to Fine Particulate Air Pollution. JAMA, 287 (9), 1132. https://doi.org/10.1001/jama.287.9.1132., **2002**.

Eitel, J.U.H., Höfle, B., Vierling, L.A., Abellán, A., Asner, G.P., Deems, J.S., Glennie, C.L., Joerg, P.C., LeWinter, A.L., Magney, T.S., Mandlburger, G., Morton, D.C., Müller, J., Vierling, K.T. Beyond

3-D: The new spectrum of lidar applications for earth and ecological sciences. Remote Sensing of Environment 186, 372–392. https://doi.org/10.1016/j.rse.2016.08.018., **2016**.

Cairo, F.; Di Liberto, L.; Dionisi, D.; Snels, M. Understanding Aerosol–Cloud Interactions through Lidar Techniques: A Review. Remote Sensing, 16 (15), 2788. https://doi.org/10.3390/rs16152788., **2024**.

Sun, K.; Dai, G.; Wu, S.; Reitebuch, O.; Baars, H.; Liu, J.; Zhang, S. Effect of Wind Speed on Marine Aerosol Optical Properties over Remote Oceans with Use of Spaceborne Lidar Observations. *Atmospheric Chemistry and Physics*, *24* (7), 4389–4409., **2024.**

Chen, W.; Liu, J.; Hou, X.; Zang, H.; Wan, Y.; Zhu, X.; Ma, X.; Chen, D.; Li, R. Spaceborne Aerosol and Carbon Dioxide Detection Lidar (ACDL) Status and Progress; Springer, pp 97–107., **2023**.

Yang, H.; Zhu, X.; Qiu, D.; Fang, Z.; Hu, Y.; Li, X. Research of Two Dust Transport Pollution in Northern China in 2023: Perspectives from LiDAR and Multi Source Data. Atmospheric Pollution Research, 102441., **2025**.

Song, Rui, Adam Povey, and Roy G Grainger, 'Characterization of Dust Aerosols from ALADIN and CALIOP Measurements', *Atmospheric Measurement Techniques*, 17.8, pp. 2521–38., **2024**.

Eckert, C.; Hernandez-Jaramillo, D. C.; Medcraft, C.; Harrison, D. P.; Kelaher, B. P. Drone-Based Measurement of the Size Distribution and Concentration of Marine Aerosols above the Great Barrier Reef. Drones, 8 (7), 292., **2024**.

Li, C., Liu, M., Hu, Y., Wang, H., Xiong, Z., Wu, W., Liu, C., Zhang, C., Du, Y., Investigating the vertical distribution patterns of urban air pollution based on unmanned aerial vehicle gradient monitoring. Sustainable Cities and Society 86, 104144. https://doi.org/10.1016/j.scs.2022.104144., **2022**.

Zhou, C., Liu, Y., He, Q., Zhong, X., Zhu, Q., Yang, F., Huo, W., Mamtimin, A., Yang, X., Wang, Y., Meng, L., Dust Characteristics Observed by Unmanned Aerial Vehicle over the Taklimakan Desert. Remote Sensing 14, 990. https://doi.org/10.3390/rs14040990., **2022**.

Girdwood, J. Optical Measurement of Airborne Particles on Unmanned Aircraft., **2023**.

Yang, H.; Zhu, X.; Fang, Z.; Qiu, D.; Hu, Y.; Tian, C.; Ming, F. Study on the Vertical Distribution and Transport of Aerosols in the Joint Observation of Satellite and Ground-Based LiDAR. *Atmosphere*, *15* (2), 240. https://doi.org/10.3390/atmos15020240., **2024.**

Kuang, Z.; Liu, D.; Wu, D.; Wang, Z.; Li, C.; Deng, Q. Parameter Optimization and Development of Mini Infrared Lidar for Atmospheric Three-Dimensional Detection. *Sensors*, *23* (2), 892. https://doi.org/10.3390/s23020892., **2023.**

Yang, H.; Fang, Z.; Cao, Y.; Xie, C.; Zhou, T.; Wang, B.; Xing, K.; Lolli, S. Impacts of Transboundary Dust Transport on Aerosol Pollution in the Western Yangtze River Delta Region, China: Insights Gained From Ground-Based Lidar and Satellite Observations. *Earth and Space Science*, *8* (3), e2020EA001533. https://doi.org/10.1029/2020EA001533., **2021.**

Zhang, Z.; Kuang, Z.; Yu, C.; Wu, D.; Shi, Q.; Zhang, S.; Wang, Z.; Liu, D. Trans-Boundary Dust Transport of Dust Storms in Northern China: A Study Utilizing Ground-Based Lidar Network and CALIPSO Satellite. *Remote Sensing*, *16* (7), 1196. https://doi.org/10.3390/rs16071196., **2024.**

Xie, C.; Zhao, M.; Wang, B.; Zhong, Z.; Wang, L.; Liu, D.; Wang, Y. Study of the Scanning Lidar on the Atmospheric Detection. *Journal of Quantitative Spectroscopy and Radiative Transfer*, *150*, 114–120. doi:10.1016/j.jqsrt.2014.08.023., **2015.**

Wang, Y.; Wang, H.; Qin, Y.; Xu, X.; He, G.; Liu, N.; Miao, S.; Lu, X.; Wang, H.; Fan, S. Measurement Report: Nocturnal Subsidence behind the Cold Front Enhances Surface Particulate Matter in Plains Regions: Observations from the Mobile Multi-Lidar System. *Atmos. Chem. Phys.*, *24* (4), 2267–2285. https://doi.org/10.5194/acp-24-2267-2024., **2024.**

Zhang, S., Zhou, Z., Ye, C., Shi, J., Wang, P., Liu, D., Analysis of a Pollution Transmission Process in Hefei City Based on Mobile Lidar. EPJ Web Conf. 237, 02006. https://doi.org/10.1051/epjconf/202023702006., **2020**.

Lv, L.; Liu, W.; Zhang, T.; Chen, Z.; Dong, Y.; Fan, G.; Xiang, Y.; Yao, Y.; Yang, N.; Chu, B. Observations of Particle Extinction, PM2. 5 Mass Concentration Profile and Flux in North China Based on Mobile Lidar Technique. *Atmospheric Environment*, *164*, 360–369., **2017.**

Wang, M.; Zhu, T.; Zheng, J.; Zhang, R. Y.; Zhang, S. Q.; Xie, X. X.; Han, Y. Q.; Li, Y. Use of a Mobile Laboratory to Evaluate Changes in On-Road Air Pollutants during the Beijing 2008 Summer Olympics. *Atmos. Chem. Phys.*, **2009**.

Megie, G., *Laser Remote Sensing: Fundamentals and Applications*. Wiley, New York., **1985**.

Qiu, D.; Qiu, D.; Wu, B.; Gu, M.; Zhu, M. Hierarchical Control of Trajectory Planning and Trajectory Tracking for Autonomous Parallel Parking. *IEEE Access*, *9*, 94845–94861. doi:10.1109/ACCESS.2021.3093930., **2021.**

Wang, S., Levin, M.W., Caverly, R.J., Optimal parking management of connected autonomous vehicles: A control-theoretic approach. Transportation Research Part C: Emerging Technologies 124, 102924. https://doi.org/10.1016/j.trc.2020.102924., **2021.**

Tu, A., Wang, Zhenzhu, Wang, Zhifei, Zhang, W., Liu, C., Zhu, X., Li, J., Zhang, Y., Liu, D., Weng, N., Characterizing a Heavy Dust Storm Event in 2021: Transport, Optical Properties and Impact, Using Multi-Sensor Data Observed in Jinan, China. Remote Sensing 14, 3593. https://doi.org/10.3390/rs14153593., **2022**.

Xiao, D., Wang, N., Chen, S., Wu, Lingyun, Müller, D., Veselovskii, I., Li, C., Landulfo, E., Sivakumar, V., Li, J., Che, H., Fang, J., Zhang, K., Wang, B., Chen, F., Hu, X., Li, X., Li, W., Tong, Y., Ke, J., Wu, Lan, Liu, C., Liu, D., Simultaneous profiling of dust aerosol mass concentration and optical properties with polarized high-spectral-resolution lidar. Science of The Total Environment 872, 162091. https://doi.org/10.1016/j.scitotenv.2023.162091., **2023**.